

Supplementary Materials for:

Giant tridimensional power responses in a T-shaped magneto-mechano-electric energy harvester

Zhonghui Yu^{a,b,c}, Jikun Yang^{e,f*}, Lei Xu^d, Jianglei Chang^a, Zhanmiao Li^c, Xiaoting

Yuan^c, Shuxiang Dong^{a*}

a. Institute for Advanced Study, Shenzhen University, Shenzhen 518051, China

b. Hubei EVE Power Co., Ltd., Jingmen 448000, China

c. School of Materials Science and Engineering, Peking University, Beijing 100871, China

d. Department of Engineering Mechanics, Tsinghua University, Beijing 100084, China

e. Department of Physics, School of Mathematics and Physics, University of Science and Technology Beijing, Beijing, China

f. State Key Laboratory for Advanced Metals and Materials, University of Science and Technology Beijing, Beijing 100083, China

Contents:

Section S1: The key parameter of the piezoceramic PZH-5H and the T-shaped ST sheet used in this work.

Section S2: The measurement method of MME responses and output performance of the T-shaped MME-EH.

Section S3: The mechanical analysis of the T-shaped MME-EH.

Section S4: Powering IoT wireless sensor and communication system by T-shaped MME-EH.

This file includes:

Figure S1. The key geometric parameter of T-shaped ST sheet used in this work.

Figure S2. The output voltage measurement method in MME responses.

Figure S3. The waveform of the applied pulse force in this work.

Figure S4. The photo of the T-shaped MME-EH used to drive 140 LEDs in real time under H_{ac} of only 1.5 Oe.

Figure S5. The measured durability characterization of the T-shaped MME-EH.

Figure S6. The simplified mechanical model of the second-order bending mode in T-shaped MME-EH.

Figure S7. The photos and illustration of magnetic field energy harvesting of the T-shaped MME-EH when a working hair dryer is approaching toward it along x (i), y (ii), and z (iii) direction, respectively.

Figure S8. The FEA analysis of the 3D-direction AC stray magnetic field caused vibrational mode in T-shaped MME-EH.

Table. S1 Basic piezoelectric parameters of the commercial PZT-5H ceramic.

Table S2. Power consumption of the elements of the commercial IoTs in this work.

Video S1. The T-shaped MME-EH used to drive 140 LEDs in real time under H_{ac} of 1.5 Oe.

Video S2. The vibration and the generated output voltage of the T-shaped MME-EH when a working hair dryer is approaching toward it.

Video S3. The T-shaped MME-EH under a hair dryer induced magnetic field radiation is used to power a Bluetooth that is then used to communicate with a cell phone.

Video S4. The operation of the wireless sensor and its communication system.

Section S1: The key parameter of the piezoceramic PZH-5H and the T-shaped ST sheet used in this work

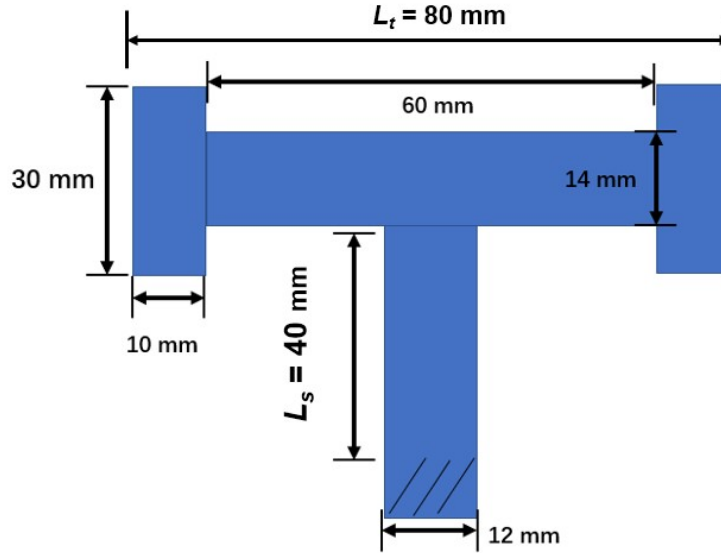


Figure S1. The key geometric parameter of the T-shaped ST sheet used in this work.

The thickness of the T-shaped ST sheet is 0.3 mm.

Table. S1 Basic piezoelectric parameters of the commercial PZT-5H ceramic.

Materials	d_{33}	g_{33}	e_{33}	$\tan\delta$	k_p	Q_m	T_c	ϵ
PZT-5H	750	20.6	21.24	4.2 %	0.76	70	180	5000

Commercial piezoceramic PZT-5H exhibits superior comprehensive properties (relatively high piezoelectric coefficient and low loss), which would be in favor of the enhancement of output power in the proposed T-shaped MME-EH.

Section S2: The measurement method of MME responses and output performance of T-shaped MME-EH.

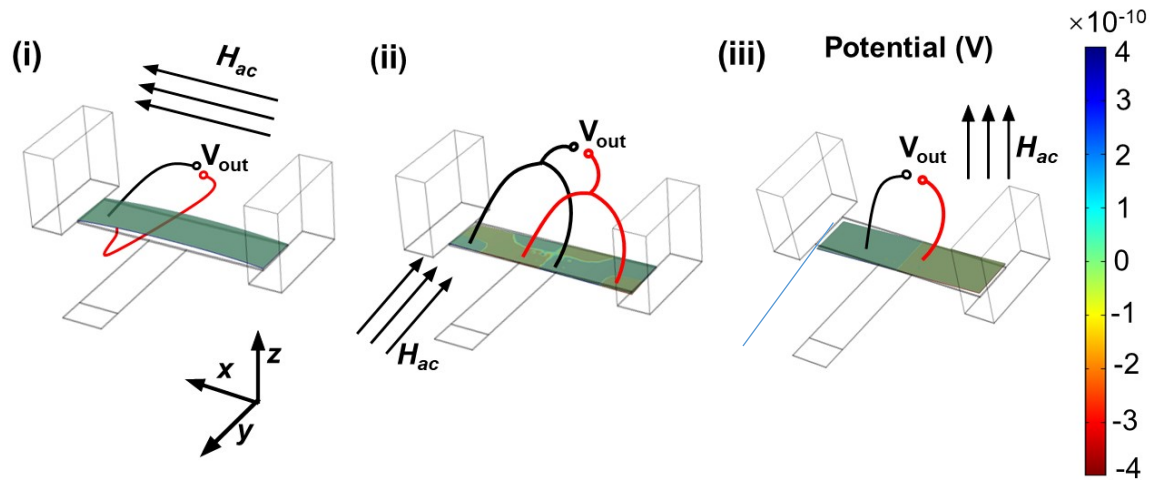


Figure S2. The output voltage measurement method in MME responses.

Under the applied H_{ac} along x direction, the T-shaped MME-EH was excited to operate in bending mode. The induced AC output voltage from the piezoceramic plate in T-shaped MME-EH was recorded by a digital oscilloscope. Under the applied H_{ac} along y or z direction, T-shaped MME-EH was excited to operate in twist modes. While the coated electrode on the piezoceramic plate was divided into several parts according to the simulated electrical potential distribution, as shown in Figure S2(ii) and S2(iii); for example, the red line and the black line are the two terminals for leading out of two different output AC voltages, respectively. In Figure S2 (ii), even though the six potential regions were formed, we only use four main potentials of them to lead out of the output voltages. It is because the stress induced potential from remaining two electrode areas near the central parts of the T-shaped MME-EH are relatively small.

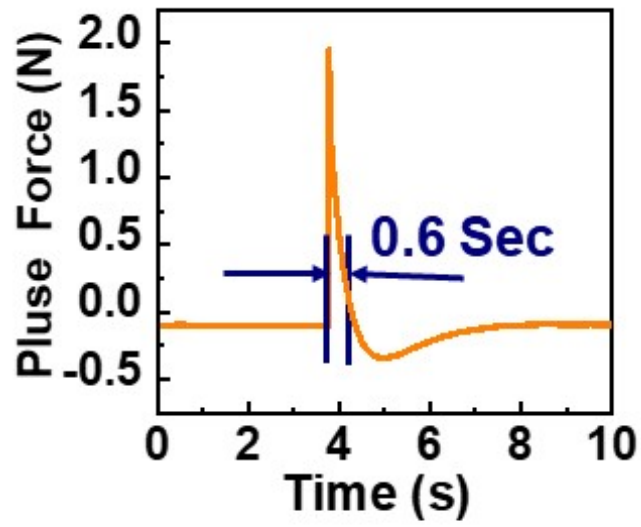


Figure S3. The waveform of the applied pulse force in this work.

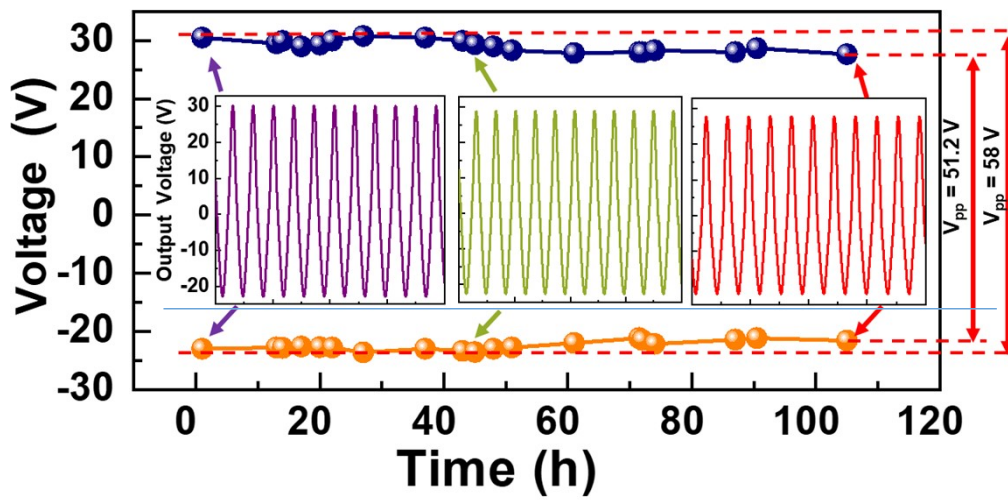


Figure S4. The measured durability characterization of the T-shaped MME-EH. After 120 hours continual operation under $H_{ac} = 1$ Oe, the efficiency decreases by $\sim 22\%$.

Section S3: The mechanical vibration analysis of the T-shaped MME-EH.

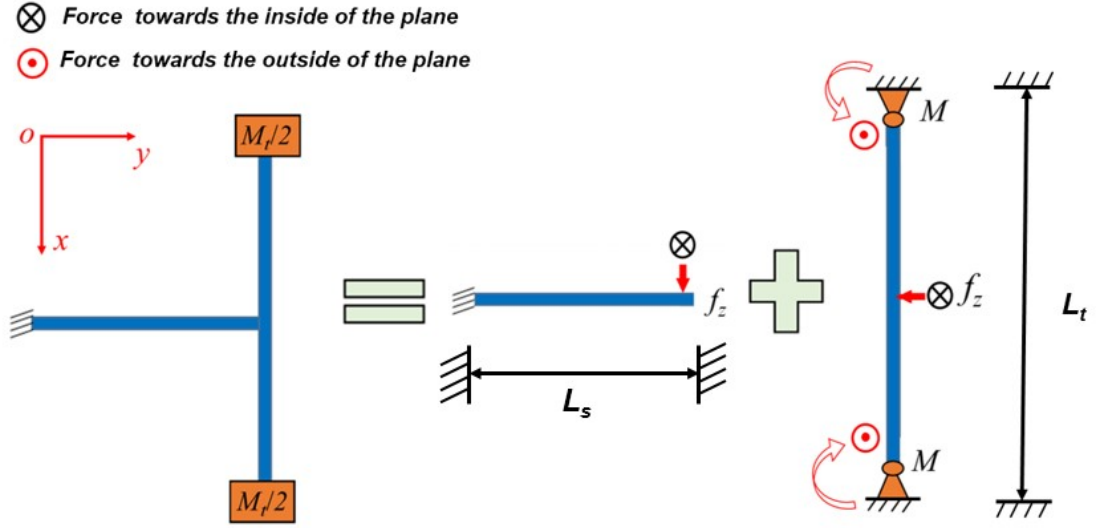


Figure S5. The simplified mechanical model of the second-order bending mode in T-shaped MME-EH.

According to the deflection result calculated by FEA, the vibrational mode of the longitudinal beam can be simplified as the first-order bending mode of the cantilever beam with one-end fixed, while the transverse beam can be simplified as the first-order bending mode of one cantilever beam with two-end simply supported. The displacement distribution w function of the transverse beam at second-order bending mode is

$$w(x,t) = q(t) \sin \frac{\pi}{L_t} x \quad (S1)$$

where the $q(t)$ represents the maximum displacement of the transverse beam, and L_t is the length of the transverse beam. Its velocity function v (dw/dt) can be written as:

$$v(x,t) = \dot{q}(t) \sin \frac{\pi}{L_t} x \quad (S2)$$

where the dot representing the time derivative. Let the mass line per unit length of the magnet to be M_x . The kinetic energy of the transverse beam is:

$$T = \int_0^{L_t} \frac{1}{2} \rho A v^2(x) dx + \int_0^{\frac{L_t}{8}} \frac{1}{2} M_x v^2(x) dx + \int_{\frac{7L_t}{8}}^{L_t} \frac{1}{2} M_x v^2(x) dx$$

$$= \frac{1}{2} \left(\frac{1}{2} m_{tb} + 0.0498 m_t \right) \dot{q}(t)^2 \quad (S3)$$

where ρ and A are the density and cross section of the ST sheet, respectively; the length of the magnet mass is taken as $L_t/8$, and m_{tb} is the mass of the transverse beam. Here, transverse beam is simplified as uniform cross section.

Similarly, the equivalent mass of the longitudinal beam can be found to be $\frac{33}{140} m_s$. Then, the equivalent mass m_{eq} of the T-shaped MME-EH can be obtained as

$$m_{eq} = \frac{33}{140} m_s + \frac{1}{2} m_{tb} + 0.0498 m_t \quad (S4)$$

where m_s is the mass of the longitudinal beam, and m_t is the sum weight of the magnet masses attached at two tip ends of transverse beam. In above simplified model, the transverse beam and longitudinal beam in the T-shaped MME-EH can be considered to be parallel connected, the equivalent stiffness of the parallel-connected transverse beam and longitudinal beam is:

$$K_{eq} = K_s + K_t = \frac{3EI_s}{L_s^3} + \frac{48EI_t}{L_t^3} \quad (S5)$$

Next, to evaluate the magneto-mechanical coupling in bending mode T-shaped MME-EH, the maximum deflection in transverse beam is analyzed. The bending moment equation in the in-phase bending mode can be written as

$$\begin{cases} EI_s w_s''(y) = f_z (L_s - y), & 0 \leq y \leq L_s \\ EI_t w_t''(x) = M + \frac{f_z}{2} x, & 0 < x \leq \frac{L_t}{2} \\ EI_t w_t''(x) = M + \frac{f_z}{2} x - f_z \left(x - \frac{L_t}{2} \right), & \frac{L_t}{2} \leq x \leq L_t \end{cases} \quad (S6)$$

where the M the bending moment generated by magnet mass attached at tip end of transverse beam, and E , I and w are Yong's model of the ST sheet, cross sectional moment of inertia and the deflection in T-shaped MME-EH. The subscripts s and t denote longitudinal and transvers beam, respectively. f_z is the reaction force caused by longitudinal beam. L_s and L_t are the length of the longitudinal beam and transverse beam respectively; w_s'' and w_t'' are the second derivative of the beam's deflection of the longitudinal beam and transverse beam in bending mode, respectively. The rotation angle equation is:

$$\left\{ \begin{array}{l} EI_s w_s'(y) = f_z L_s y - \frac{1}{2} f_z y^2 + A_1, \quad 0 \leq y \leq L_s \\ EI_t w_{t1}'(x) = Mx + \frac{1f_z}{22} x^2 + C_1, \quad 0 \leq x \leq \frac{L_t}{2} \\ EI_t w_{t2}'(x) = Mx + \frac{1f_z}{22} x^2 - \frac{f_z}{2} \left(x - \frac{L_t}{2}\right)^2 + C_2, \quad \frac{L_t}{2} \leq x \leq L_t \end{array} \right. \quad (S7)$$

Where w_s' , and w_t' are the rotation angle of the longitudinal beam and transverse beam respectively. The deflection equation is given by:

$$\left\{ \begin{array}{l} EI_s w_s = \frac{1}{2} f_z L_s y^2 - \frac{1}{6} f_z y^3 + A_1 y + B_1, \quad 0 \leq y \leq L_s \\ EI_t w_{t1}(x) = \frac{1}{2} Mx^2 + \frac{1f_z}{62} x^3 + C_1 x + D_1, \quad 0 \leq x \leq \frac{L_t}{2} \\ EI_t w_{t2}(x) = \frac{1}{2} Mx^2 + \frac{1f_z}{62} x^3 - \frac{f_z}{6} \left(x - \frac{L_t}{2}\right)^3 + C_2 x + D_2, \quad \frac{L_t}{2} \leq x \leq L_t \end{array} \right. \quad (S8)$$

Where w_s , and w_t are the deflection of the longitudinal beam and transverse beam respectively. According to the boundary and continuity conditions of the longitudinal beam and transverse beam in T-shaped MME-EH, one can obtain:

$$\left\{ \begin{array}{l} y = 0, w_s = 0, \\ y = 0, w_s' = 0, \\ w_{t1}(x = 0) = 0, \\ w_{t2}(x = L_t) = 0, \\ w_{t1}(x = \frac{L_t}{2}) = w_{t2}(x = \frac{L_t}{2}) \\ w_{t1}'(x = \frac{L_t}{2}) = w_{t2}'(x = \frac{L_t}{2}) \end{array} \right. \quad (S9)$$

The solution of the equation (S8) is:

$$\left\{ \begin{array}{l} A_1 = 0, B_1 = 0, \\ D_1 = D_2 = 0 \\ C_1 = C_2 = -\frac{1}{2} M L_t - \frac{1f_z}{82} L_t^2 \end{array} \right. \quad (S10)$$

According to the continuity equation in T-shaped MME-EH, we have

$$w_{t1}(x = \frac{L_t}{2}) = w_s(y = L_s) \quad (S11)$$

The reaction force f_z in the equation (S8) can be easy to obtain:

$$f_z = \frac{\left(-\frac{1}{8} M L_t^2\right)}{\left(\frac{I_t}{3I_s} L_s^3 + \frac{1}{48} L_t^3\right)} \quad (S12)$$

Then, the equation (S8) can be expressed as:

$$\left\{ \begin{array}{l} w_s = \frac{f_z}{EI_s} \left(\frac{1}{2} L_s y^2 - \frac{1}{6} y^3 \right), 0 \leq y \leq L_s \\ w_{t1} = \frac{1}{EI_t} \left(\frac{1}{2} M (x^2 - L_t x) + \frac{f_z}{2} \left(\frac{x^3}{6} - \frac{L_t^2 x}{8} \right) \right), 0 \leq x \leq \frac{L_t}{2} \\ w_{t2}(x) = \frac{1}{EI_t} \left(\frac{1}{2} M (x^2 - L_t x) + \frac{f_z}{2} \left(\frac{x^3}{6} - \frac{L_t^2 x}{8} \right) - \frac{f_z}{6} \left(x - \frac{L_t}{2} \right)^3 \right), \frac{L_t}{2} \leq x \leq L_t \end{array} \right. \quad (S13)$$

The maximum deflection $w_{t \max}$ at the junction $(x = \frac{L_t}{2}, y = L_s)$ of the transverse beam and the longitudinal beam in T-shaped MME-EH is:

$$w_{t \max} = \frac{f_z L_s^3}{3EI_s} = \frac{2ML_t^2}{16EI_t + EI_s \frac{L_t^3}{L_s^3}} \quad (S14)$$

Section S4: Powering IoT wireless sensor and communication system by T-shaped MME-EH.

Table S1. Power consumption of the elements of the commercial IoTs in this work.

Element	Power Consumption (μW)
IST3055 MCU	$< 600 \mu\text{A}$ (Run mode, @1.8-5.5V supply) $< 0.5 \mu\text{A}$ (Sleep mode, @1.8-5.5V supply)
TLSR8251 Bluetooth module	5.3 mA (RX/TX mode, @1.8-3.6V supply) 1 μA (Sleep mode, @1.8-3.6V supply)
LCD screen	10-100
SHTV3 sensor IC	4.8(@2.4V supply, 1measurement/s)

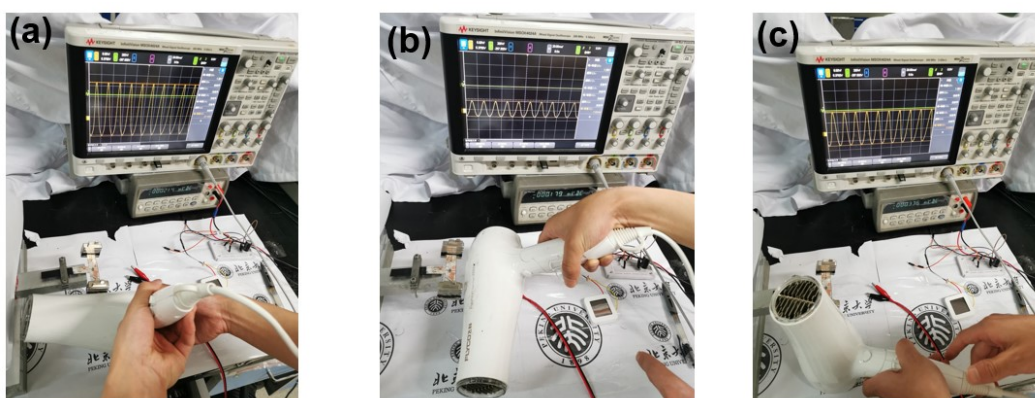


Figure S6. The photos and illustration of magnetic field energy harvesting of the T-shaped MME-EH when a working hair dryer is approaching toward it along x (i), y (ii), and z (iii) direction, respectively.

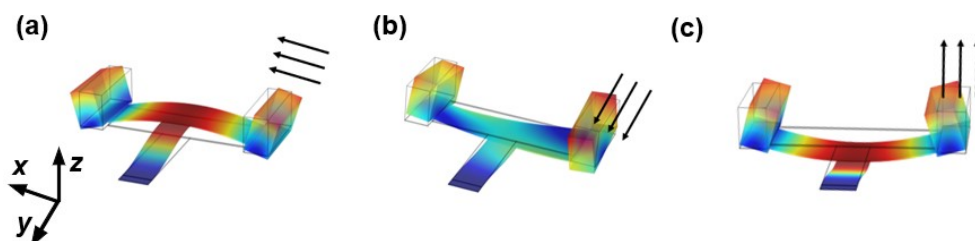


Figure S7. The FEA analyses of the 3D-direction AC stray magnetic field caused vibrational mode in T-shaped MME-EH.

